RESEARCH ARTICLE | JUNE 26 2024

Controlled ion transport in the subsurface: A coupled advection–diffusion–electromigration system *⊙*

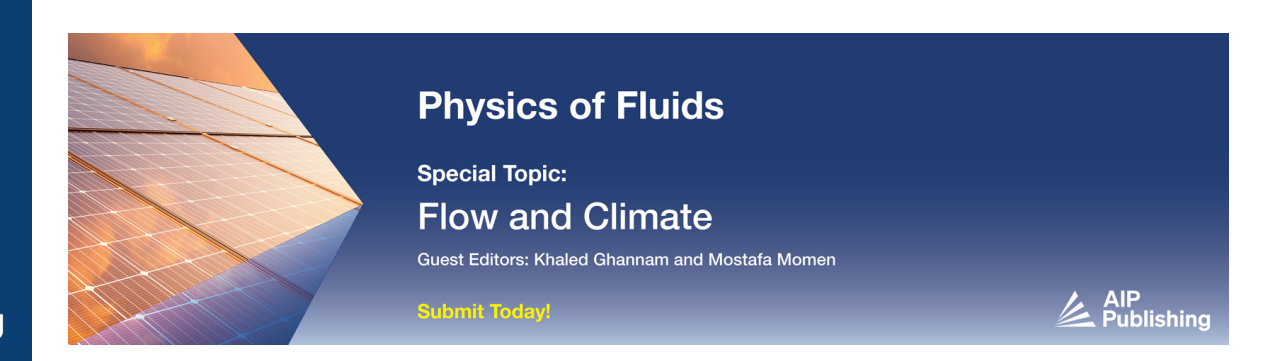
Kunning Tang **№** (a); Zhenkai Bo (b); Zhe Li (c); Ying Da Wang (c); James McClure (c); Hongli Su (c); Peyman Mostaghimi (c); Ryan T. Armstrong (c)



Physics of Fluids 36, 067137 (2024) https://doi.org/10.1063/5.0213161









Controlled ion transport in the subsurface: A coupled advection-diffusion-electromigration system

Cite as: Phys. Fluids **36**, 067137 (2024); doi: 10.1063/5.0213161 Submitted: 9 April 2024 · Accepted: 6 June 2024 · Published Online: 26 June 2024







Kunning Tang,^{1,a)} (b) Zhenkai Bo,² (b) Zhe Li,³ (b) Ying Da Wang,¹ (b) James McClure,⁴ (b) Hongli Su,⁵ (b) Peyman Mostaghimi,⁶ (b) and Ryan T. Armstrong⁶ (b)

AFFILIATIONS

- 1 School of Minerals and Energy Resources Engineering, The University of New South Wales, Sydney, NSW 2052, Australia
- ²School of Chemical Engineering, The University of Queensland, Brisbane QLD 4072, Australia

ABSTRACT

Ion transport within saturated porous media is an intricate process in which efficient ion delivery is desired in many engineering problems. However, controlling the behavior of ion transport proves challenging, as ion transport is influenced by a variety of driving mechanisms, which requires a systematic understanding. Herein, we study a coupled advection-diffusion-electromigration system for controlled ion transport within porous media using the scaling analysis. Using the Lattice-Boltzmann-Poisson method, we establish a transport regime classification based on an Advection Diffusion Index (ADI) and a novel Electrodiffusivity Index (EDI) for a two-dimensional (2D) microchannel model under various electric potentials, pressure gradients, and concentration conditions. The resulting transport regimes can be well controlled by changing the applied electric potential, the pressure field, and the injected ions concentration. Furthermore, we conduct numerical simulations in a synthetic 2D porous media and an x-ray microcomputed tomography sandstone image to validate the prevailing transport regime. The simulation results highlight that the defined transport regime observed in our simple micromodel domain is also observed in the synthetic two- and three-dimensional domains, but the boundary between each transport regime differs depending on the variation of the pore size within a given domain. Consequently, the proposed ADI and EDI emerge as dimensionless indicators for controlled ion transport, Overall, our proof-of-concept for ion transport control in porous media is demonstrated under advection-diffusion-electromigration transport, demonstrating the richness of transport regimes that can develop and provide future research directions for subsurface engineering applications.

Published under an exclusive license by AIP Publishing. https://doi.org/10.1063/5.0213161

I. INTRODUCTION

The transport of ions in an electrolyte solution through porous media plays a crucial role in a variety of engineering applications, such as heavy metal removal from soils, hydrodynamic containment removal, in situ oxidation for groundwater remediation, and the recovery of subsurface resources. The ability to control the transport of ions within the fluid is often desirable for various engineering scenarios, depending on the specific characteristics of the application and the economic importance of the ion being recovered or injected. Ion transport within the fluid can be subjected to multiple driving

mechanisms, including advection, diffusion, and electromigration. These mechanisms are visually described in Fig. 1. Advection refers to the transport of ions by the bulk movement of a fluid due to a driving pressure gradient. For diffusion, ions are transported from regions of high concentration to regions of low concentration due to Brownian motion. Finally, with electrokinetic transport (EK), an ion is transported by electromigration and electroosmotic flow (EOF). While electromigration involves the displacement of ions toward an electrode of opposite charge, EOF is a form of advective transport resulting from fluid flow induced by the applied electric field.

³Research School of Physics, The Australian National University, Canberra ACT 2601, Australia

⁴National Security Institute, Virginia Tech, Blacksburg, Virginia 24061, USA

⁵Institute of Frontier Materials, Deakin University, Geelong, VIC 3220, Australia

⁶School of Civil and Environmental Engineering, University of New South Wales, Sydney, NSW, 2052, Australia

^{a)}Author to whom correspondence should be addressed: kunning.tang@unsw.edu.au

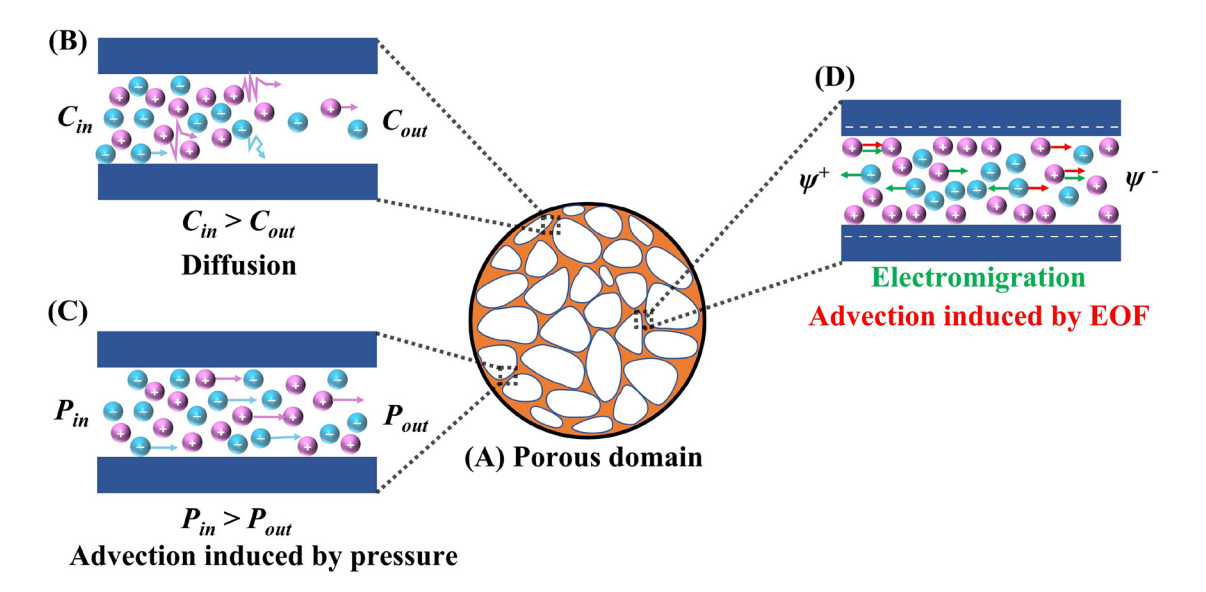


FIG. 1. Schematic description of each ion driving mechanism: (a) A porous domain; (b) ion transport due to diffusion; (c) ion transport due to advection which is induced by external hydraulic pressure; and (d) ion transport by electromigration due to an external electric field (marked by green arrows) and advection due to EOF with a charged solid surface (marked by red arrows).

In many practical scenarios, a combination of driving mechanisms occurs concurrently, impacting ion transport. For example, for EK soil remediation, the movement of ions is governed by the interplay of electromigration, electroosmotic flow (EOF), and diffusion.8 Many previous studies have investigated ion transport within the fluid under coupled transport mechanisms.⁸⁻¹³ For example, under advective-diffusive transport, the ion concentration front is sharp when the dominant transport mechanism is advection by fluid flow. In contrast, tailing effects on the concentration profile are observed when diffusion dominates the transport process, leading to undesirable outcomes, e.g., the back diffusion problem reported by Brooks et al.11 With EK transport, electromigration has been demonstrated to resolve these issues by promoting ion transport toward an electrode in combination with advective-diffusive transport.8 Examples include the removal of copper ion contaminants from sandstone¹⁴ and the delivery of permanganate oxidant to low-permeability zones. 13 Upon harnessing electromigration in these applications, other physics may contribute positively (e.g., electroosmosis that promotes oxidant delivery⁸) or negatively (e.g., advection that "overwhelms" ion electromigration 15). For the successful implementation of ion transport in the subsurface, many factors need to be considered, such as ion concentration, pressure gradient, and applied voltage field, which must be carefully designed. 16 As a result, ion transport control in multi-physics systems is challenging and often costly.

Many of the numerical models have been proposed to solve the fluid flow and ion transport under various driving mechanisms at pore-scale, such as these using finite element method, ^{18,19} volume of fluid, ^{20,21} and lattice-Boltzmann method (LBM). ^{22–25} In terms of direct simulation of 3D porous media, LBM has been commonly applied due to its inherent scalability of parallel computation and efficient handling of complex boundary conditions. ²⁶ Studies of solving advection–diffusion–electromigration using LBM are based on simultaneously solving the Poisson, Nernst–Planck, and Navier–Stokes equations in a

self-consistent scheme.^{22,27} Wang *et al.*²² studied the effect of electrically driven and pressure-driven flows on flow velocity, electro-viscous effect, and electroosmosis in homogeneous microchannels. The LBM has also been used to study EOF in a heterogeneous pore structure under different pH and zeta potential.²⁴ Such studies are examples of the successful application of LBM schemes to analyze fluid flow under advection–diffusion–electromigration.

To characterize ion transport in porous media under various scenarios dominated by physics, scaling theory is considered an ideal tool. Non-dimensional scaling theory, which refers to translating results from one scale (smaller) to another (larger) under the same dimensionless groups, has been proposed and widely used to classify flow regimes in fluid mechanics. Dimensionless numbers, such as Péclet number (describing the ratio between advective and diffusive flow), Damköhler number (describing the ratio between the mass transport rate to the intrinsic reaction), Reynolds number (describing the ratio of inertial forces to viscous forces within a fluid), and heterogeneity index (describing a characteristic length to the spatial distribution of conductivity), are well defined and serve to classify fluid flow in porous media under various controlling factors. Some well-known flow regimes that are defined using dimensionless numbers include the following:

- 1. Laminar flow and turbulent flow regime.³⁵ Laminar flow occurs at low Reynolds numbers, indicating a smooth, orderly flow pattern, while turbulent flow emerges at high Reynolds numbers, characterized by chaotic and irregular movements.
- Reaction and diffusion regime in reactive transport. The Péclet number and the Damköhler number are used to categorize dissolution patterns, such as the formation of conical wormholes versus uniform dissolution across the porous media.³⁶
- 3. Forced convection, natural convection, and mixed convection patterns.³⁷ Determined by the Grashof number and the Reynolds

number. Forced convection is driven by external forces under a higher Re. Natural convection occurs because of the buoyancy effects caused by density differences in the fluid, typically represented by a higher Grashof number.

Using these dimensionless numbers, scaling analysis helps to upscale experimental results, ^{32,38} compare research results, ^{39–41} and understand the expected flow regime. ⁴² Although scaling theory has been widely applied to characterizing fluid flow, there are only a few scaling analyses that investigate ion transport behavior within fluid in porous media. ^{8–10,43} Under scaling theory, the ion transport regimes are commonly dominated by advection and diffusion, where several regimes, such as channeling, piston, and dispersive flow, are observed through experimental and numerical studies. ⁹ The ion transport behaviors under EK have also been investigated using scaling analysis in a limited number of studies. For example, the effects of varying the electric potential on ion transport in porous media are found to be distinct from other transport mechanisms. ^{8,10}

From the literature, we can conclude that many important factors can affect ion transport in porous media.^{5,10,44} To the best of our knowledge, the coupled influences of diffusive, advective, electromigration, and electroosmotic flow have not been systematically investigated. Full-physics simulations are, therefore, a starting point to understand the coupled impact of these transport mechanics and the richness of complexity that they provide. In this paper, we aim to conduct a numerical analysis of the scaling of ion transport regimes in porous media under various electric potentials, pressure gradients, and ion concentrations. We define an Advection Diffusion Index (ADI) to characterize the ion fluxes resulting from diffusive and advective transport, which is defined as the ratio of the average ion flux due to advection and the average ion flux due to diffusion (ADI = $\frac{\text{Advectiveflux}}{\text{Diffusiveflux}}$). Similarly, we define a new dimensionless number called the Electrodiffusivity Index (EDI) to describe the ratio between ion fluxes due to electromigration and diffusion (EDI = $\frac{\text{Electromigrationflux}}{\text{Diffusiveflux}}$). First, we benchmark the resulting transport regimes according to visual observations of transport simulations in a simple 2D microchannel model under various electric potentials, pressure fields, and concentration conditions. Furthermore, numerical simulations are conducted in a synthetic 2D porous medium and a 3D domain built from an x-ray microcomputed tomography (micro-CT) sandstone image to validate the benchmarked ion transport regimes observed from the microchannel model. Finally, we investigate the effects of pore size variation on the ion transport regime. All simulations are carried out with an opensource solver OPM/LBPM using the lattice Boltzmann-Poisson method (LBPM). The validation of this model can be found in Ref. 27. Furthermore, to facilitate future applications in the field, we quantified the transport patterns by studying the ion transport efficiency and ion breakthrough time. Overall, our aim is to provide a systematic understanding of ion transport within a fluid for an advection-diffusionelectromigration system.

The presented work is structured as follows. Section II explains the coupling equation for solving the advection-diffusion-electromigration system using LBPM. This section also introduces the models and images used for simulations. Section III shows the characterization of 4 ion transport regimes from a microchannel model. Then, two dimensionless numbers are proposed to characterize the transport regimes. Furthermore, this transport regime is further demonstrated in 2D/3D porous media. The last part of Sec. III shows the implications

of the transport regimes for engineering applications. Finally, Sec. IV concludes several findings and suggests potential directions for future research.

II. METHODS AND MATERIALS

A. Theoretical background and numerical methods

The governing equations for an advection-diffusion-electromigration system include three coupled equations: (1) the Nernst-Planck equation for ion transport driven by chemical and electric potentials, (2) the Navier-Stokes equation for the flow of an electrolyte solution carrying ions driven by hydrodynamic potential, and (3) the Poisson equation that couples the ionic distribution to compute the electric potential, which in turn is fed into the Nernst-Planck and Navier-Stokes equations.

More specifically, the transport of an ion species is modeled by the Nernst-Planck equation,

$$\frac{\partial C_i}{\partial t} + \nabla \cdot \mathbf{J}_i = 0, \tag{1}$$

where C_i is the concentration of the *i*th ion, and J_i is the associated mass flux, given by

$$J_i = J_i^d + J_i^a + J_i^e, \tag{2}$$

where the net diffusive flux, J_i^d , advection flux, J_i^a , and electromigration flux, J_i^e are defined as

$$J_i^d = -D_i \nabla C_i,$$

$$J_i^a = uC_i,$$

$$J_i^e = -\frac{z_i D_i}{V_T} \nabla \psi C_i,$$
(3)

where D_i is the diffusivity of the *i*th ion, z_i is the ion algebraic valency, and $V_T = k_B T/e$ is the thermal voltage, where k_B is the Boltzmann constant and e is the electron charge.

The Nernst-Planck equation is solved in the pore spaces, and a non-flux boundary condition was applied to model the bounce-back of ions of the ion-solid interface,

$$\mathbf{n}_{s} \cdot \mathbf{J}_{i} = 0, \quad \text{for } \mathbf{x} \in \partial \Omega,$$
 (4)

where n_s is the unit normal vector of the solid surface.

The flow of the electrolyte solution that carries ion species is governed by the incompressible Navier–Stokes equations and the conservation of mass,

$$\nabla \cdot \boldsymbol{u} = 0,$$

$$\frac{\partial \boldsymbol{u}}{\partial t} + \boldsymbol{u} \cdot \nabla \boldsymbol{u} = -\frac{1}{\rho_0} \nabla p + \nu \nabla^2 \boldsymbol{u} + \frac{\boldsymbol{F}}{\rho_0},$$
(5)

where ${\it u}$ is the fluid velocity vector, ρ_0 is the fluid density, p is the fluid pressure, ν is the kinematic viscosity, and ${\it F}$ is the body force, which in this study is essentially due to an external electric field.

The standard no-slip boundary condition is applied to the fluid-solid interface. In addition, when the thickness of the EDL is much smaller than the characteristic length of the simulation domain (i.e., the resolution of an input image), an electroosmotic velocity boundary condition is introduced in the EDL, which ignores the detailed flow between the solid surface and slipping plane and analytically calculates

the velocity at the solid according to the local zeta potential of the solid surface. In this work, we adopted the widely used Helmholtz–Smoluchowski (HS) equation,

$$\boldsymbol{u} = -\frac{\epsilon \zeta}{\mu} \nabla_T \psi \quad \text{for } \boldsymbol{x} \in \partial \Omega,$$
 (6)

where ψ is the electric potential within the fluid, Ω denotes the fluid domain, ζ is the local zeta potential at the solid surface, ϵ is the permittivity of the electrolyte solution, and ∇_T is the tangential part of the gradient operator, perpendicular to the orientation of the solid surface. In short, when the EDL is not resolvable due to the input image resolution, the electroosmotic velocity boundary is applied to replace the electrical body force in Eq. (5).

The electric potential resulting from the ion transport is solved by the Poisson equation,

$$\nabla^2 \psi = -\frac{\rho_e}{\varepsilon_r \varepsilon_0},\tag{7}$$

where ε_0 is the permittivity of vacuum, and ε_r is the dielectric constant of the electrolyte solution. The net charge density ρ_e (C/m³) is calculated based on the ion concentration,

$$\rho_e = \sum_i F z_i C_i, \tag{8}$$

where the sum runs over all ionic species and F is Faraday's constant given by $F = eN_A$, where N_A is Avogadro's number. The Poisson equation couples the Nernts-Planck and Navier-Stokes equations together, as it takes charge concentration as an input, solves for the electric potential that in turn affects ion transport, and leads to a Coulomb force in the fluid transport. For regions where the net charge is non-zero, an induced electrical body force that can drive the fluid flow in the Navier-Stokes equation is given by

$$F_e = \rho_o E = -\rho_o \nabla \psi. \tag{9}$$

Normally, a nonzero charge distribution occurs in the EDL; when the EDL is not resolvable, i.e., the body force F_e reduces to the HS boundary condition in Eq. (6). On the solid surface, the boundary condition for the electric potential is typically specified in two forms: (a) the surface charge density σ_e and (b) the surface potential ψ_s . When the EDL is unresolvable, the surface potential reduces to the zeta potential. The former is a Neumann-type boundary condition given by

$$n_s \cdot \nabla \psi = -\frac{\sigma_e}{\varepsilon_r \varepsilon_0}$$
 for $\mathbf{x} \in \partial \Omega$, (10)

and the latter is a Dirichlet-type boundary given by

$$\psi(\mathbf{x}) = \psi_s \quad \text{for } \mathbf{x} \in \partial\Omega,$$
 (11)

where ψ_s is a user-specified electric potential of the solid surface. To solve the aforementioned coupled equations in a porous media domain, we adopted the commonly used LBM, due to its inherent scalability of parallel computation and efficient handling of complex boundary conditions. The numerical details of the LBM model implemented can be found in Sec. I in the supplementary material, and the validation of the governing equations can be found in. ^{26,27} Simulations were performed on a local workstation with a 64-core CPU, 24 GB of

GPU memory, and 256 GB of RAM. All simulations were computed on the GPU due to a faster computational speed than the CPU.

B. Simulation of domain-synthetic porous media

Electrokinetic applications range from unconsolidated soil to consolidated sedimentary rocks where pore sizes could impact the transport behavior. We start with a simple 2D microchannel model to study the transport regimes under different pressures, concentrations, and electrical gradients. This helps in (1) establishing the type of transport regime that can develop and (2) testing our proposed dimensionless groups to categorize the transport behavior. Next, synthetic 2D porous media and 3D sandstone images obtained from micro-CT are used to validate the existence of the transport regimes in porous media with varying pore sizes. Sections II B 1–II B 3 will introduce how our modeling domains are built and their basic characteristics.

1. Microchannel model domain

We start with a homogeneous 2D microchannel model (the size of a single path is constant) to benchmark the ion transport regime. Herein, a microchannel model with the size of 90 \times 150 pixels is created consisting of four microchannels with apertures of 3, 4, 7, and 11 μ m, as shown in Fig. 2(a). The four microchannels are the same length. Thus, the channel size is the only factor that influences the ion transport.

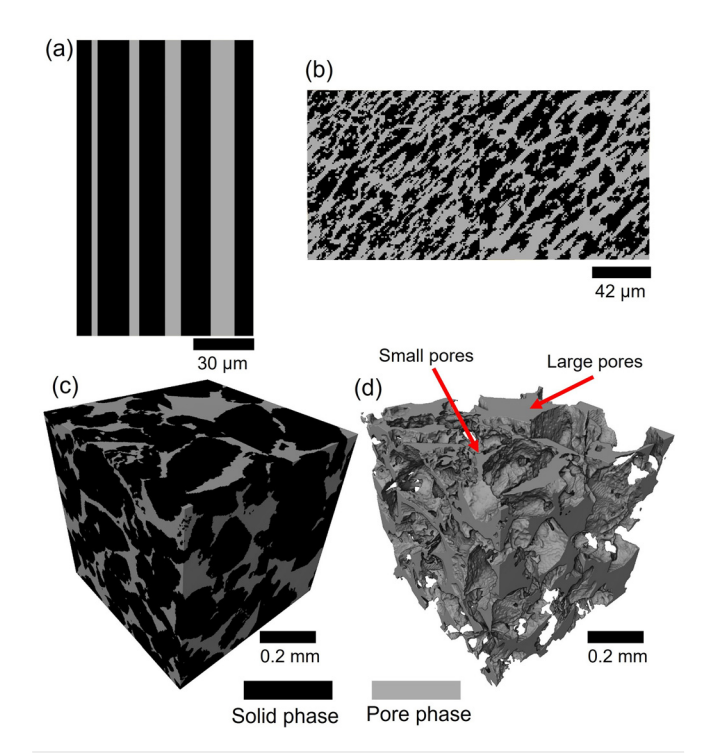


FIG. 2. Synthetic porous media (a) 2D microchannel model, resolution $= 1 \, \mu m$; (b) 2D synthetic porous media with different pore size, resolution $= 1 \, \mu m$; (c) binary segmentation of 3D concatenated micro-CT image of the bentheimer sandstone, resolution $= 2.5 \, \mu m$; and (d) pore space of the bentheimer sandstone.

2. Synthetic 2D porous model

The microchannel model provides constant pore size over the domain length and does not permit ion flux from one pore to another. To build a porous media that mimics essential features of real rocks and sediments, such as the radius of the pores, porosity, tortuosity, and the contrast between large and small pores, we use a sequential indicator simulation algorithm. During sequential indicator simulation, categorical indicators of "pore" and "solid" are populated to each grid (pixel) of the domain based on predefined statistics of that pore space, which includes the length of pore space in major and minor directions and the azimuth angle of pore spaces to the vertical spaces. As such, the size of the populated pore space is within a specified range and provides contrast when two generated porous domains are combined.

Two porous media with average pore sizes, small $(3 \, \mu m)$ and large $(5 \, \mu m)$, are generated. We then concatenate the small-pore media with the large-pore media to obtain a synthetic porous model with a contrast in the pore-size distributions. As shown in Fig. 2(b), the 2D model has two sections with an overall size of 256×127 pixel with a pixel resolution of $1 \, \mu m$. The porous media on the left has narrower pore spaces connected from top to bottom, ensuring connectivity between the boundaries and each pore. The other porous section on the right shows pore spaces wider than those of the left section and presents a similar connection pattern between the boundaries and each pore. Such a model will facilitate the observation of ion transport behavior in both small and large pore spaces.

3. 3D Sandstone micro-CT image

A 3D micro-CT image of Bentheimer sandstone with a voxel resolution of 2.5 μm is used to explore ion transport regimes in a common type of porous geological rock. 46-49 To generate a sandstone image with various pore size distributions, we first crop a subdomain with a voxel size of $128 \times 256 \times 256$. Then, the corresponding length of the subdomain is increased two times, resulting in an increase in the size of the voxel from 2.5 to 5 μ m (the number of voxel increases from 128 \times 256×256 to $256 \times 512 \times 512$). A $128 \times 256 \times 256$ voxel domain is trimmed from the $256 \times 512 \times 512$ domain and concatenated to the raw $128 \times 256 \times 256$ domain to generate a final domain with 256^3 voxel. Finally, assuming a constant voxel resolution of 2.5 μ m for the entire domain, we generate a 3D sandstone image with variation in the pore size distributions. The 3D binary segmented sandstone image is shown in Fig. 2(c). The pore sizes can be observed in Fig. 2(d), where one side of the domain has substantially larger average pore sizes than the other, which are 14 and 10.5 μ m on average, respectively. We consider sandstone as it provides a clear basis to verify transport mechanisms and demonstrate proof-of-concept while ensuring that the spatial resolution of the porous media is sufficient to resolve the physics.

C. Calculation of dimensionless numbers and simulation configuration

The definition of ADI and EDI is expressed in the following equations:

$$ADI = \frac{J_{zi}^a}{J_{xi}^d},\tag{12}$$

$$EDI = \frac{J_{zi}^e}{J_{zi}^d},\tag{13}$$

where z refers to the main transport direction; herein, the main driving forces are applied in the z-direction. J_{zi}^a refers to the advective flux of ion i. J_{zi}^d refers to the diffusive flux of ion i, and J_{zi}^e refers to the electromigration flux of ion i.

Various initial and boundary ion concentrations, electric potentials, and pressure gradients are applied to these simulations. Herein, boundary refers to the model's top (inlet) and bottom (outlet) open boundaries, and the surrounding boundaries of the 2D and 3D models have no transport. As a result, the ion transport (flux) from the inlet to the outlet boundary is defined as positive, while the opposite is defined as negative. It should be noted that in this study, ADI and EDI refer to the dimensionless directional number where both positive and negative directions of ion transport are considered. Therefore, EDI and ADI can be positive or negative based on the direction of the flux. This is important since for the given system, transport mechanisms can operate in opposite directions.

For ionic conditions, we adopt the same ion types as those used in back diffusion remediation technology, 8,13 where a fixed concentration of potassium permanganate solution (KMnO₄) mixed with hydrochloric acid (HCl) is injected from the inlet boundary, and the domains are initially saturated with sodium chloride solution (NaCl) and HCl. At the outlet boundary, the same concentration as the initial concentration of NaCl mixed with the HCl solution is used. The boundary and initial concentration used for all simulations are summarized in Table S1. Other simulation parameters, such as ion diffusivity, are summarized in Table S2 in supplementary material. It is noted that all of the following results and analyses are based on the permanganate ion that is negatively charged.

The permanganate ion is transported into the models under three transport mechanisms, which correspond to diffusion, electromigration, and advection. With the initial and boundary conditions of ion transport applied herein, the net diffusive flux is always from inlet to outlet. Electromigration flux depends only on the setting of the electric potential. The permanganate ion moves to the outlet if the anode is set at the outlet, and vice versa. The advection flux of ions is caused by fluid flow, which mainly contains two driving mechanisms—one is the fluid flow caused by a pressure gradient, and another term is the fluid flow caused by the EOF, which occurs due to the existence of an EDL when the electric potential is applied to a charged material's surface. The thickness of the EDL is characterized by the Debye length. In our simulation, when the ionic concentration is set as shown in Table S2, the Debye length is around 4 nm, which is small compared to the average pore size of our domains.²⁴ Therefore, the EDL is assumed to be a thin layer, and the HS equation [Eq. (6)] and the zeta potential are used to describe electroosmosis. The local zeta potential on the solid surface is strongly dependent on pH and weakly dependent on ionic concentration.^{24,51} Considering that all our simulations are performed at constant pH (pH=6), the zeta potential of the solid (quartz) is assumed to be constant at $-20 \,\mathrm{mV}^{52}$ This assumption is reasonable in situations where the electrical double layer (EDL) is not resolvable and external transport mechanisms are applied. The driving force on the ions due to the zeta potential is governed by electro-osmosis, which is significantly smaller than the driving forces of electromigration, diffusion, and advection.²⁷ At each time step, ion fluxes due to the three transport mechanisms and net ion flux are calculated, from which the ADI and EDI are calculated. Finally, the ion transport regime is characterized by visualizing the ion flux vs time.

TABLE I. Description of the identified ion transport regimes.

Ion transport regimes	Description
Large channeling	Ion transport primarily occurs through the larger channels/pres, with less or halted transport in smaller channels/pores.
Uniform transport	Ion transport occurs uniformly through each channel/pore regardless of channel/pore size
Small channeling	Ion transport primarily occurs through the smaller channels/pores, with less transport in the larger
	channels/pores.
No transport	Ion flux in all channels/pores disappears (zero net ion flux and/or negative net ion flux), or ion stops transporting into all channels.

III. RESULTS AND DISCUSSION

A. Ion transport regime benchmark

First, the ion transport regimes are characterized according to visual observations of net ion flux in the synthetic model. In this subsection, we simulate the advection–diffusion–electromigration transport of ions in the 2D microchannel model. We identified four ion transport patterns from the simulation results and benchmarked the ion transport regimes accordingly, which are large channeling, uniform transport, small channeling, and no transport. A brief description of each regime can be found in Table I.

Large channeling occurs when ion transport is advection dominant. This occurs when ADI is positive and relatively large compared to EDI, which means that the hydraulic pressure is applied from top to bottom of the model and is the main transport mechanism compared to diffusion and electromigration. With large channeling, ion transport mostly occurs through the larger channels, with less transport in the smaller channels. The typical transport pattern is shown in Fig. 3(a).

Additionally, when an electric potential is applied with the anode at the top of the model and the cathode at the bottom of the model, meaning the EDI is negative, the permanganate ion has a uniform flux of electromigration toward the anode (from bottom to top). Under the condition where advection dominates over electromigration, this uniform electromigration transport will have less influence on the ion transport in large channels, but the advection flux in small channels is canceled out by the uniform electromigration transport. Moreover, such a transport pattern will start to change again when the electric potential is increased, resulting in more electromigration and less advection. Under this condition, there is no net ion transport through the small channels, and net ion transport in the large channel is reduced, as shown in Fig. 3(d). We define the transport patterns in Figs. 3(a) and 3(d) as large channeling, since the ion transport occurs primarily through the larger channels, with minimal or stopped transport in the smaller channels.

A uniform transport pattern occurs where EDI dominates over ADI or both are small compared to the net diffusive flux. A typical uniform transport pattern is presented in Fig. 3(b), uniform transport delivers high transport efficiency compared to large channeling (both small and large channels are swept by ion fluxes). For an advection-diffusion system, uniform transport occurs only when diffusion dominates the transport. With an external electric potential, uniform transport can occur with both electromigration and diffusion. One can alter the ion concentration and the electric potential to change the flux of the uniform transport. The channel length between large channels and small channels is also a factor that affects the ion transport regime;

however, it is ignored in the 2D microchannel model, where all channels have the same length. The impact of pore size variation is discussed in the synthetic 2D porous media and 3D sandstone domain.

Small channeling prevails as the negative ADI increases and becomes the main transport mechanism over the EDI. Applying a large pressure gradient on the 2D microchannel in the opposite direction (from bottom to top) to the uniform ion transport will counterbalance the ion fluxes in the large channels first. Consequently, since the negative flux by pressure is larger in the middle of the channel and smaller along the solid surface as a result of viscous flow, negative net ion flux starts to occur at the middle part of the large channel. The typical small channeling pattern is shown in Fig. 3(c). When EDI becomes negative, advection and electromigration flux counterbalance the net diffusive flux. Small channeling can still exist when the net diffusive flux is comparable to negative advection flux and electromigration flux. However, no transport appears to occur when the advection and electromigration driven fluxes are increased. In some cases of large and small channeling transport regimes, ion fluxes in the minor transport paths (small channels during large channeling or large channels during small channeling) would first disappear due to the counterbalance of transport mechanisms in the opposite direction. A transition transport pattern is defined between the small channeling and the no transport regimes.

Ion fluxes in all channels will disappear once the counterbalance dominates. Herein, we define both zero net ion flux and negative net ion flux as the no transport regime. Figure 3(e) shows an extension case to Fig. 3(d) with an increase in the electric potential. For this case, the advection and diffusion flux at smaller channels are fully counterbalanced by the electromigration flux. In contrast, at the largest channel, ions can be transported into the channel at an early step because the advection flux is higher compared to the small channel, the diffusion flux is high at a high concentration gradient, and the electromigration flux is low since less ion is transported into the channel. However, with the transport of ions into this channel, the concentration gradient reduces, and electromigration increases. As a result, the ion transport becomes negative and no ions can further transport into this channel, where only an early cluster remains positive net flux. We define this as no transport. Additionally, Fig. 3(f) shows the no transport regime originating from large channeling and uniform transport. We define this observation of transport behavior as no transport.

After characterizing the ion transport patterns in the advection—diffusion—electromigration system, we conducted 40 simulations using various combinations of the ADI and EDI on the 2D microchannel model and defined the transport pattern based on visual observation.

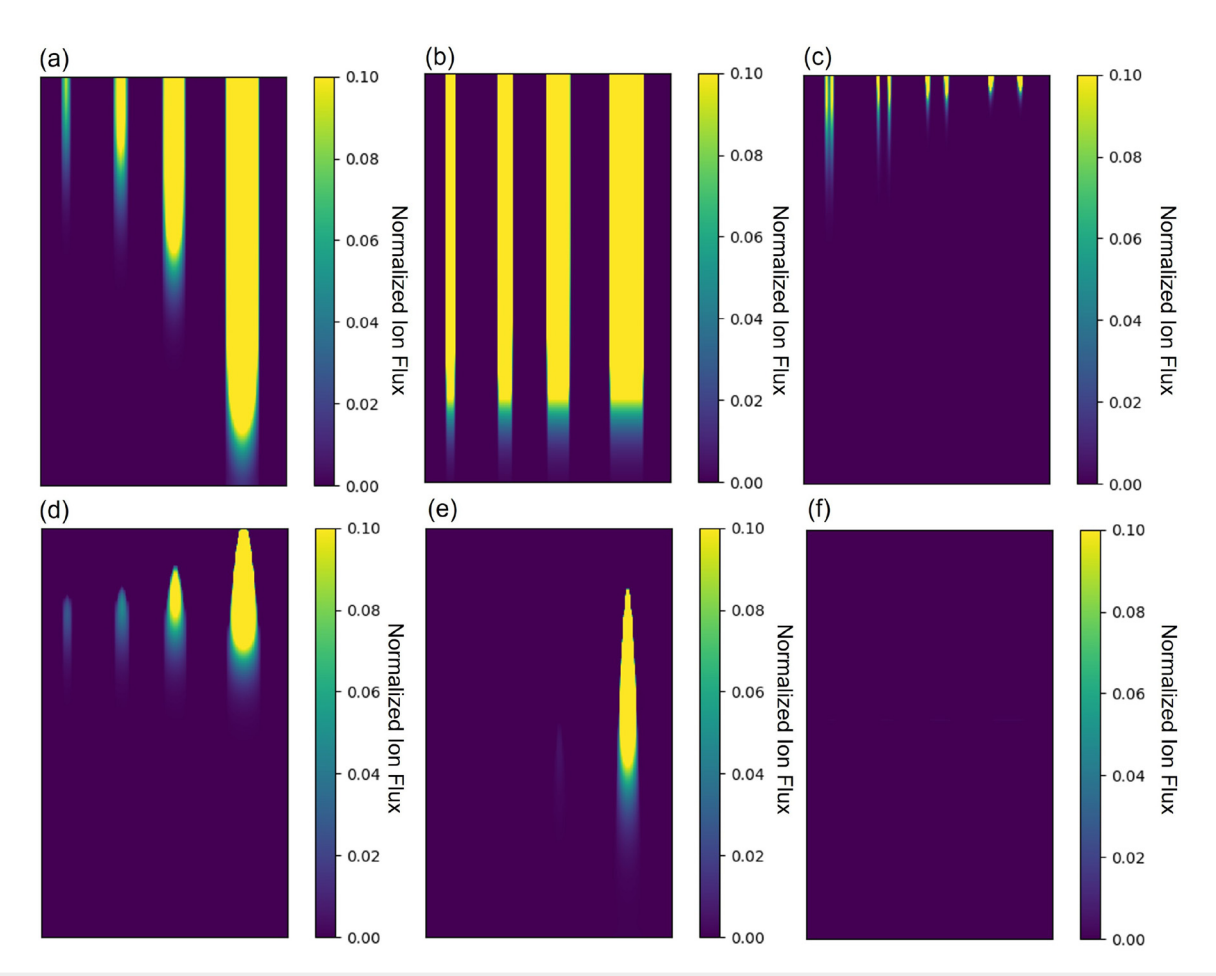


FIG. 3. Typical net ion flux transport regimes identified in 2D microchannel model: (a) Large channeling, EDI = 0, ADI = 29.61; (b) uniform transport, EDI = 1.93, ADI = -9e - 4; (c) small channeling, EDI = 9.5e - 6, ADI = -0.95; (d) large channeling, EDI = -2.5, ADI = 1; (e) no transport, EDI = -20.78, ADI = 10.84; and (f) no transport, EDI = -2, ADI = 1e - 3.

The simulation results are represented graphically in Fig. 4. On the basis of the simulation results, the ion transport regime is defined. A positive value of the dimensionless number means that the driving force moves ions from the inlet to the outlet.

In the following, we will explain the transport regimes that occurred in each quadrant of the phase diagram presented in Fig. 4.

- In the first quadrant, the EDI and ADI are both positive. When ADI is large enough, the transport is always large channeling, while when the EDI is dominant and ADI is small, uniform transport can be achieved.
- In the second quadrant, EDI is positive and ADI is negative. A symmetrical uniform transport region exists where the EDI is dominant and ADI is small. Small channeling is located where a negative ADI refers to the counterbalance of flux in the large channels.
- In the third quadrant, the EDI and ADI are both negative; when
 the net diffusive flux can still counterbalance the negative flux
 caused by the negative EDI and ADI, small channeling exists.
 With a further increase in ADI, the flux region in the large channel is further reduced, increasing diffusion to the region that still

has flux (transport along the solid surface), such as the small channel in Fig. 3(c), where the flux of ions along the solid surface of the larger channel is greater than that of a small channel. At a certain ADI value, the transport in the small channel stopped, while there is still flux along the solid surface in the large channel. We name this region the transition zone. With further increases in the EDI and ADI, no transport occurs.

• In the fourth quadrant, the EDI is negative and ADI is positive. The no transport pattern occurs when the electromigration is more dominant than the advection and diffusion. When advection begins to dominate, large channeling occurs. A uniform transport region in the third and fourth quadrants is defined when the net diffusive flux and the electromigration flux are counterbalanced; however, the net diffusive flux is still larger than the electromigration flux.

B. Observation in 2D and 3D Domains

Next, porous media with different pore sizes and tortuosity are used to investigate ion transport under advection–diffusion–electromigration

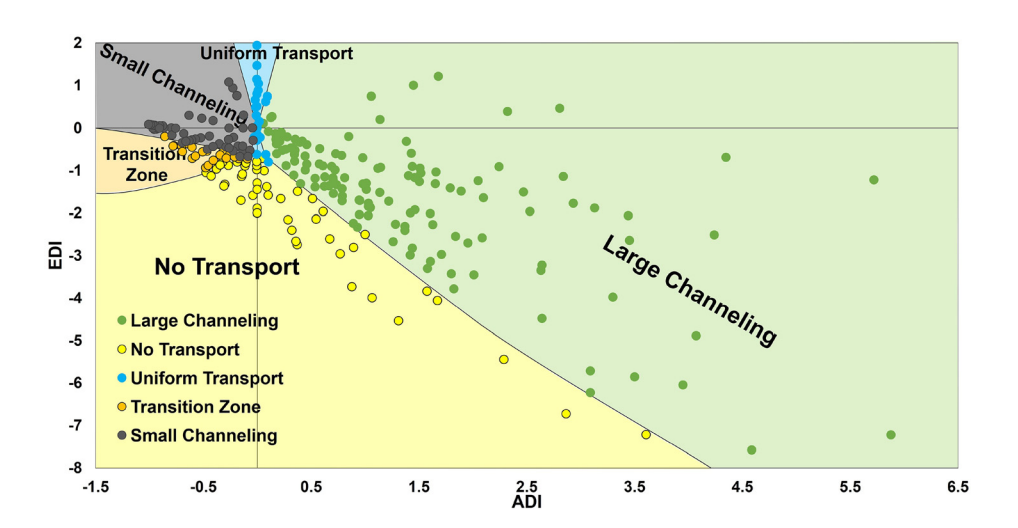


FIG. 4. Illustration of advection-diffusionelectromigration transport regime map. The figure shows the simulation points with different ADI and EDI in the 2D microchannel model. Transport regimes can be defined based on these points.

in more complex domains than the previously presented 2D microchannel.

1. Ion transport regime on synthetic 2D porous media

To generate the ion transport regimes for the 2D porous media, we perform 20 simulations that contain EDI and ADI combinations that span the four quadrants of the phase diagram presented previously. Figure 5 shows the transport regimes of 20 simulations at the same time step. We observe four transport regimes: (1) large channeling, (2) uniform transport, (3) small channeling, and (4) no transport. Large channeling can be observed in the right column where positive ADI was used. With decreasing EDI from positive to negative (from 1.1 to -45.7), the transport in the low porosity zone is

counterbalanced by the electric potential, making the large channeling more apparent. These observations of the large channeling regime fit with the benchmark transport regime defined in Fig. 4(b). With a decrease in ADI to around 0.4, large channeling becomes less apparent. Meanwhile, with decreasing EDI, more uniform transport can be observed, such as the one with EDI = -0.8 and Pe = 0.4. When ADI is further reduced, ion transport is dominated by diffusion or electromigration and is counterbalanced by pressure in the negative ADI quadrant. Therefore, uniform transport and small channeling occurred (EDI = 0, Pe = 6e - 12 and EDI = -1.5, Pe = 3e - 4). For the negative ADI and EDI regions, the transport regimes are mainly small channeling and no transport (EDI = -0.8, Pe = -1.1 and EDI = -1.2, Pe = -1.1), which matches the fourth quadrant of our benchmark transport regime. Furthermore, with negative ADI and

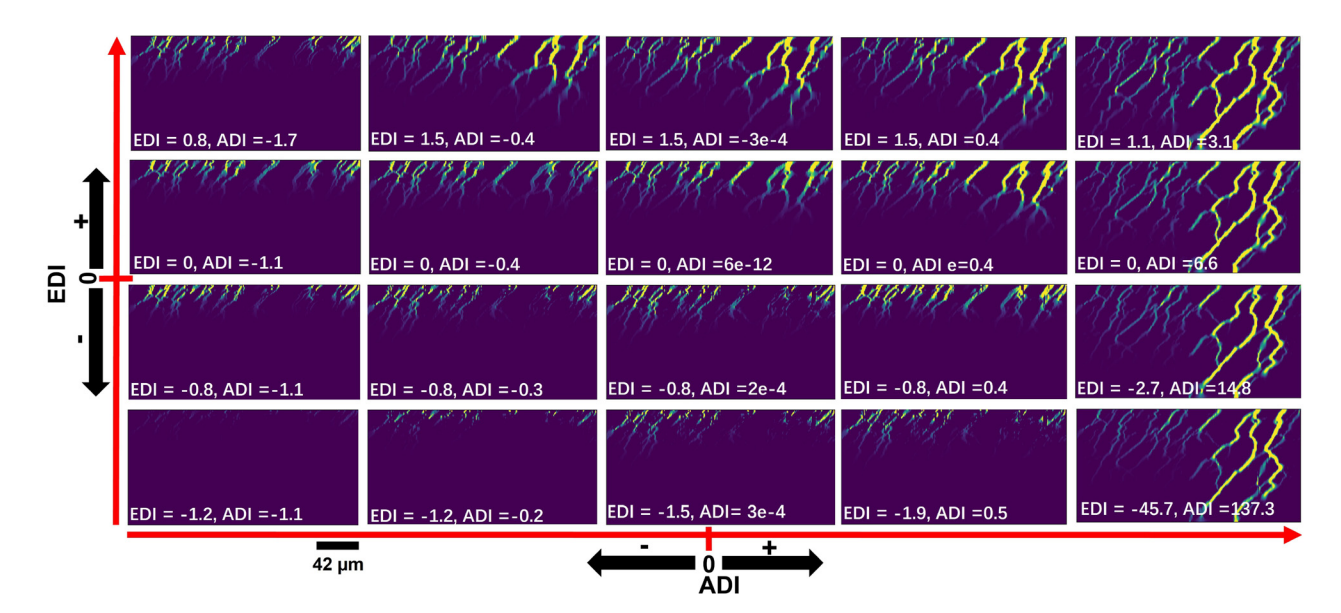


FIG. 5. Ion transport regime for the 2D synthetic porous media. All ion transports presented here are at time = 0.51 s. The ion flux in each subplot is normalized to 0–1 within itself

large positive EDI, small channeling is also observed (Pe=-1.7 and EDI=0.8), which matches the third quadrant transport regime in Fig. 4(b). It is noted that the boundary of the transport regime in the synthetic 2D porous media is different from that obtained in the 2D microchannel due to the influence of the pore size variation in the synthetic 2D porous media. A good example is when EDI=0 and Pe=6e-12, uniform transport is observed with a 2D microchannel where the pore size remains the same for each channel; meanwhile, weak large channeling is achieved with the synthetic 2D porous media, as shown in Fig. 5.

To further compare and quantify these transport regimes, we analyze the occupied pore size distribution and the concentration map for a typical large channeling, uniform transport, and small channeling

at the same time step, as shown in Fig. 6. Here, we study the size of pores that are occupied by ions with a concentration greater than 1% of the inlet concentration.⁵³ Based on the ion flux pattern, we use the watershed transform algorithm to separate each pore that is occupied by ions.⁵⁴ We then calculate the pore size based on the pore's equivalent diameter. From the size distribution map, we find that greater than 64% of the ion-occupied pores for small channeling have an equivalent diameter of less than 3 pixels, which is twice that for the uniform transport and large channeling regimes. The maximum diameter of the ion-occupied pores for small channeling is around 6 pixels. However, 16% of the ion-occupied pores for uniform transport and 28% of the ion-occupied pores for large channeling had diameters greater than 6 pixels. For uniform transport, the maximum diameter

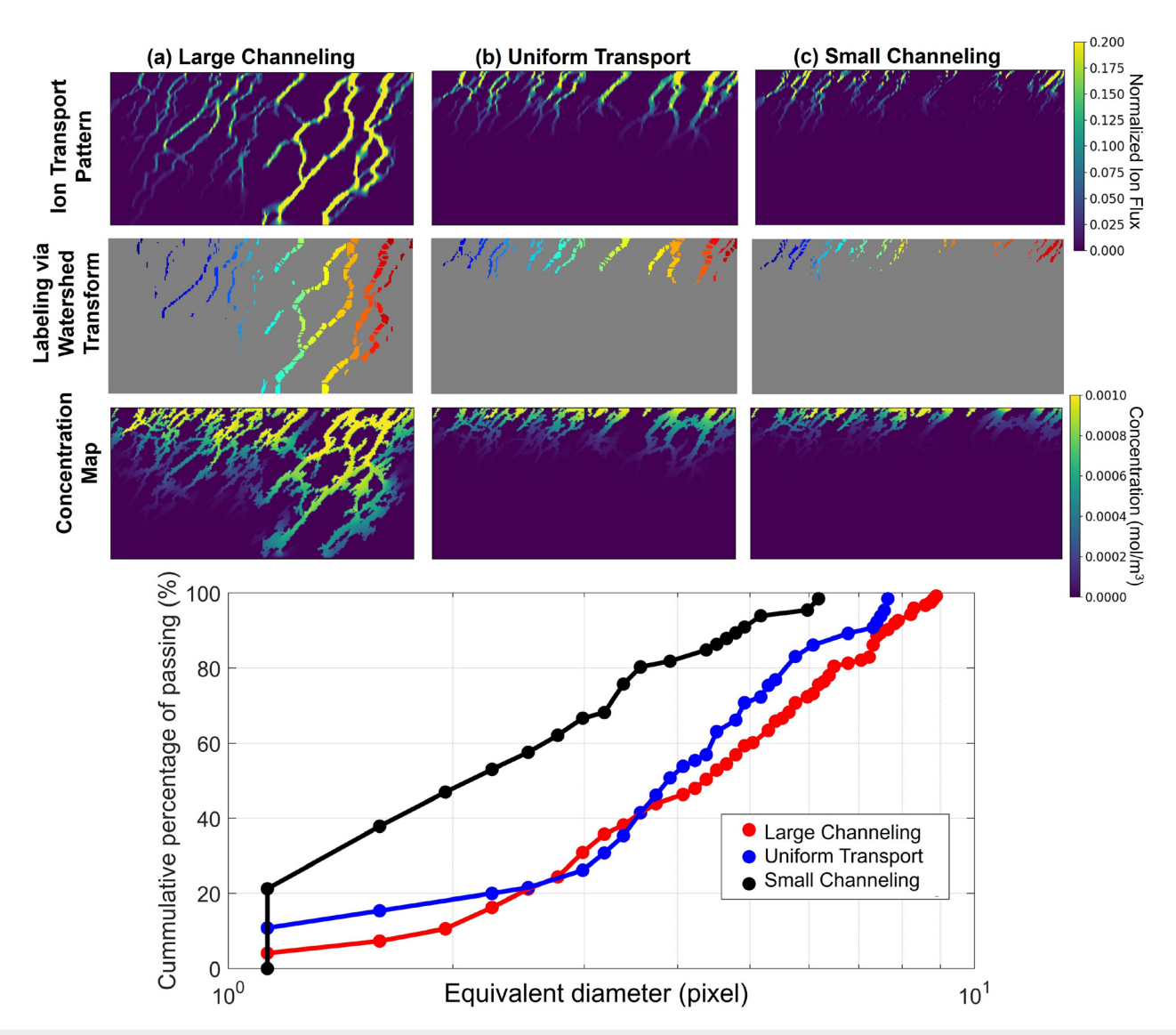


FIG. 6. Occupied pore size distribution and the visualization of concentration map of three typical transport regimes in the advection–diffusion–electromigration system: (a) EDI = 1.1, Pe = 3.1; (b) EDI = 0, Pe = 6e - 12; and (c) EDI = 0.8, Pe = 1.7. The pore size is generated using the watershed transform algorithm. The occupied pore size is calculated using the equivalent diameter method and plotted in the unit of pixel.

of the ion-occupied pore is around 7.8 pixels. At 3.8 pixels in size, which is approximately half the maximum size, 50% of the pores are greater than 3.8 pixels. Therefore, the pore size distribution map of each transport regime can be used to quantify the transport regime we visually defined.

In addition, we studied the transport regimes at breakthrough. Breakthrough is defined when 1% of the inlet ion concentration is observed at the outlet. Six different cases, including small channeling, uniform transport, and large channeling, are simulated until the breakthrough. The results are reported in Fig. 7. When both EDI and ADI are zero, the ion transport is diffusion-only, and uniform transport should occur. However, due to the variation in pore size, the ion transport path in the larger pore region is shorter than in the smaller pore regions; thus, the breakthrough occurs first at the outlet of the large pore region. The efficiency of ion transport (as a quantification parameter) is the ratio of the pore volume with an ion concentration larger than 1% of the inlet ion concentration to the overall pore volume. The ion transport efficiency is 75.5% at breakthrough

time = 1.36 s for ion transport under diffusion only. By giving a large positive EDI with a negative ADI, such as the case in Fig. 7(c), the movement of ion increases and the breakthrough time decreases to 0.69 s. Because of the early breakthrough, the ion transport efficiency also decreased. By increasing the negative ADI to be comparable to the EDI, as shown in case Fig. 7(e), the fast movement of ion in the large pore region is counterbalanced by negative advective flux. Therefore, a more uniform transport is formed with the highest ion transport efficiency (83.2%); a longer breakthrough time (1.83 s) is also observed. In another case where advection is dominant and the EDI is negative [Fig. 7(b)], large channeling occurs, and breakthrough at t = 0.16 s occurs at the large pore region with the lowest ion transport efficiency (52.3%). Furthermore, small channeling can be observed when the EDI is slightly less than the ADI, such as in Fig. 7(d), negative advective flux counterbalanced the ion flux in the larger pore region, and thus breakthrough occurs in the smaller pore region. The ion transport efficiency is 65.0%, but more time is required for the ion to breakthrough (t = 2.44 s) compared to the large channeling cases. With a

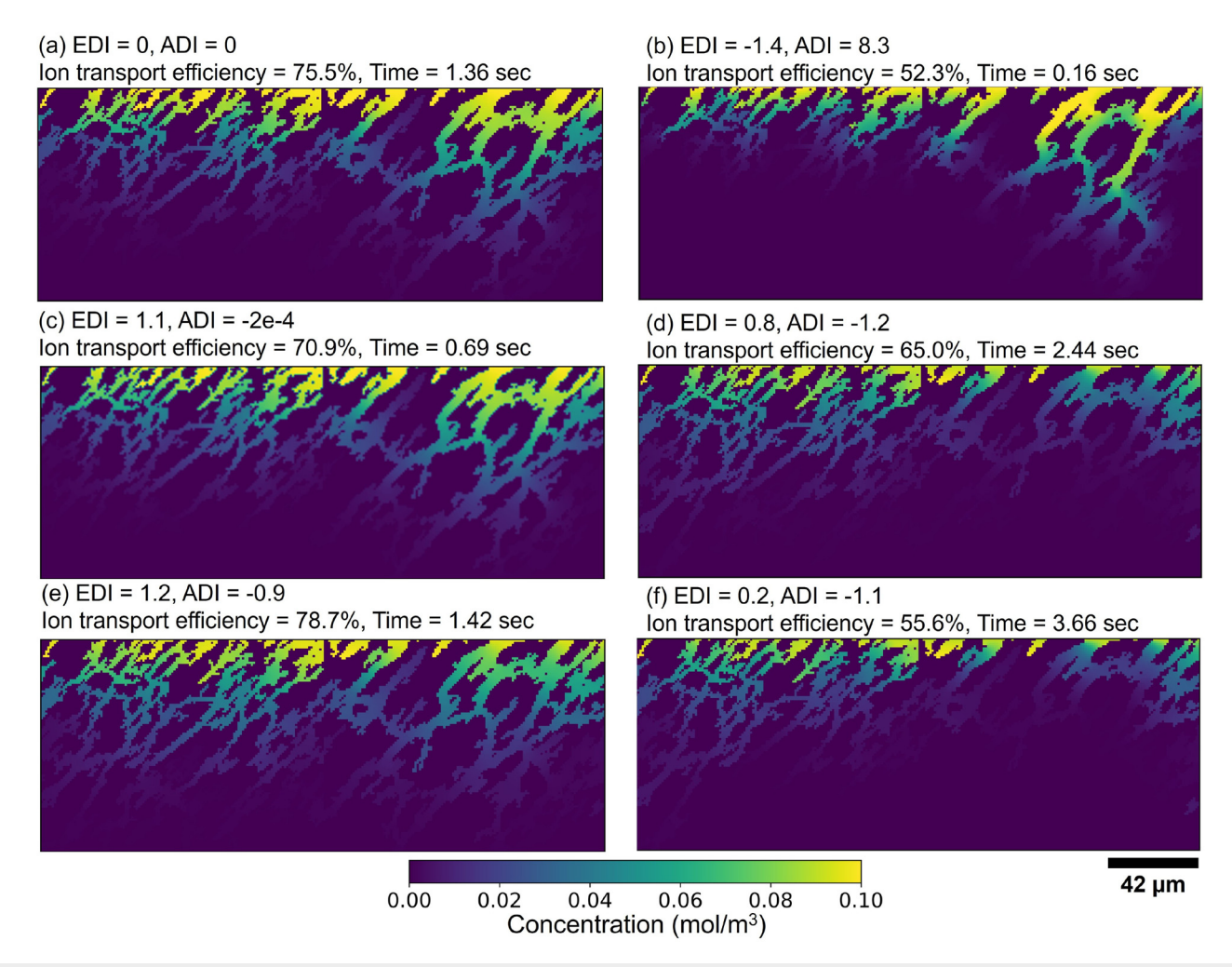


FIG. 7. Ion transport regimes and the ion transport efficiency at breakthrough times. Large channeling, uniform transport, and small channeling are observed with different EDI and ADI combinations.

further decrease in the EDI, the negative advection flux becomes dominant compared to positive diffusion and electromigration transport [Fig. 7(f)], apparent small channeling is formed, and ion transport efficiency decreases. Ion transport is slower with less EDI, so the time for breakthrough is longer.

Combined with the observations from the microchannel model, ion transport under the diffusion or electromigration-dominant condition would tend to be uniform transport when the geometry of the pores would not vary the transport path (tortuosity) to the outlet of the simulation domain (such as those in the microchannel model). This is because the driven force as the ion concentration gradient and electric potential distributions, for diffusion and electromigration, respectively, are not affected by the geometry of the pore spaces. In contrast, when the transport path is lengthened more by the small pores compared to the pores with greater sizes, uniform transport (under the same EDI) could become large channeling as the ion concentration would breakthrough first through the larger pores (channels, with shorter transport path). This is similar to a condition that advection is dominant where the fluids in large pores suffer from smaller frictions. Therefore, when ADI is dominant over EDI and they are in the same direction, large channeling occurs. Otherwise, when ADI and EDI are in opposite directions, small channeling occurs as the transport in the large pores would be suppressed by the negative advection heavier than the pores with smaller sizes. On the basis of these analyses, we find that, by using the electric potential as a component of the driving force in the advection-diffusion system, any of the desired ion transport behavior can be achieved, which provides flexibility when dealing with different applications.

2. Ion transport regimes on a 3D sandstone

Finally, the ion transport regime is tested on a 3D sandstone domain. For the 3D micro-CT domain, the porosity and mean equivalent diameter for the subdomain with larger pores is 0.36 and 14 μ m, while that for the subdomain with smaller pores is 0.27 and 10.5 μ m. Three cases including large channeling, uniform transport, and small channeling are simulated until 1% of inlet ion concentration reaches the outlet (breakthrough). The results are shown in Fig. 8. Large channeling occurs in Fig. 8 (a), where the EDI is negative and the ADI is positive and dominant. The majority of ions move through the high porosity region and breakthrough occurs at 2.9 s with a final ion transport efficiency of 54.4%. The paired EDI and ADI of the three time steps fall into the large channeling transport regime in the fourth quadrant, as benchmarked in Fig. 4. For Fig. 8(b), the direction of the pressure gradient and electric potential are reversed compared to Fig. 8(a), resulting in a positive EDI and negative ADI. A uniform transport pattern is observed where ions are uniformly distributed. The breakthrough time is delayed compared to large channeling because the ions move slower with negative ADI. The efficiency of ion transport at breakthrough for uniform transport is 84.8%. In the last case [Fig. 8(c)], the pressure gradient is increased, and the electric potential is decreased compared to Fig. 8(b); resulting in small channeling. By comparing the small channeling case to the large channeling case, we discover that ions do not move through the main transport channel in Fig. 8(a) and instead move through the subdomain with low porosity. For ion breakthrough, small channeling takes more than twice as much time as the other two transport regimes. Combined with the breakthrough time of uniform transport, there is a trade-off between the enhanced volumetric displacement efficiency via the utilization of different ion transport regimes and the time efficiency of the resulting ion transport through the porous media. For the case of small channeling, the simulation results fall within the third quadrant of the ion transport regime presented in Fig. 4. Overall, from the 3D simulations, we confirm that the observed ion transport regimes match the benchmarked transport regimes in Fig. 4.

C. Implications for engineering applications

Regarding engineering applications, accurately estimating and optimizing ADI and *EDI* to target the preferred transport regime prior to any simulation or experiment would be vital. However, the present definitions of the ADI and EDI in Eqs. (12) and (13), which rely on flux parameters, are not ideal. This is because it is challenging to directly estimate these fluxes before the experiment and/or simulation. To address this, we further define the ADI and EDI in a way that includes a characteristic length scale term and can be estimated before/during the experiment and/or simulation. This is done by using the diffusive, advection, and electromigration flux defined in Eq. (3). The new definitions are shown in the following equations:

$$ADI = \frac{u\bar{C}_i}{-D_i\nabla C_i} \tag{14}$$

and

$$EDI = \frac{\frac{z_i D_i}{V_T} (\nabla \psi) \bar{C}_i}{D_i \nabla C_i} = \frac{z_i (\nabla \psi) \bar{C}_i}{V_T \nabla C_i},$$
(15)

where \boldsymbol{u} is the average fluid flow velocity, \bar{C}_i is the average ith ion concentration through the system, D_i is the diffusivity of the ith ion, z_i is the ion algebraic valency, V_T is the thermal voltage is defined as $V_T = k_B T/e$, where k_B is the Boltzmann constant and e is the electron charge, ∇C_i can be defined as $\nabla C_i = (\partial C_i)/\partial x$, and it can also be defined as $\nabla C_i = (C_{i,in} - C_{i,out})/L$, where L is the characteristic length, $\nabla \psi$ can also be defined as $\nabla \psi = \psi/L$, where ψ is the applied external electric potential. Eqs. (14) and (15) can be further written as Eqs. (16) and (17) by replacing the ∇C_i and $\nabla \psi$ with the characteristic length term as follows:

$$ADI = \frac{uL\bar{C}_i}{-D_i(C_{i,in} - C_{i,out})}$$
(16)

and

$$EDI = \frac{z_i \psi \bar{C}_i}{V_T (C_{i,in} - C_{i,out})}.$$
 (17)

Each term in Eqs. (16) and (17) can be estimated before/during a simulation and/or experiment. Specifically, D_i is known for each ion, L can be estimated for a given domain, \mathbf{u} , $C_{i,in}$, and $C_{i,out}$ can be measured before/during simulation and experiment, \bar{C}_i can also be estimated depending on the system, for example, it can be the initial concentration of the system or the average value of $C_{i,in}$ and $C_{i,out}$, and V_T can be estimated based on temperature. These equations thus allow the screening of transport regimes on any representative (scalable) elementary volume of a porous electro-kinetic domain. Further extending these dimensionless parameters to a continuum-scale formulation, for

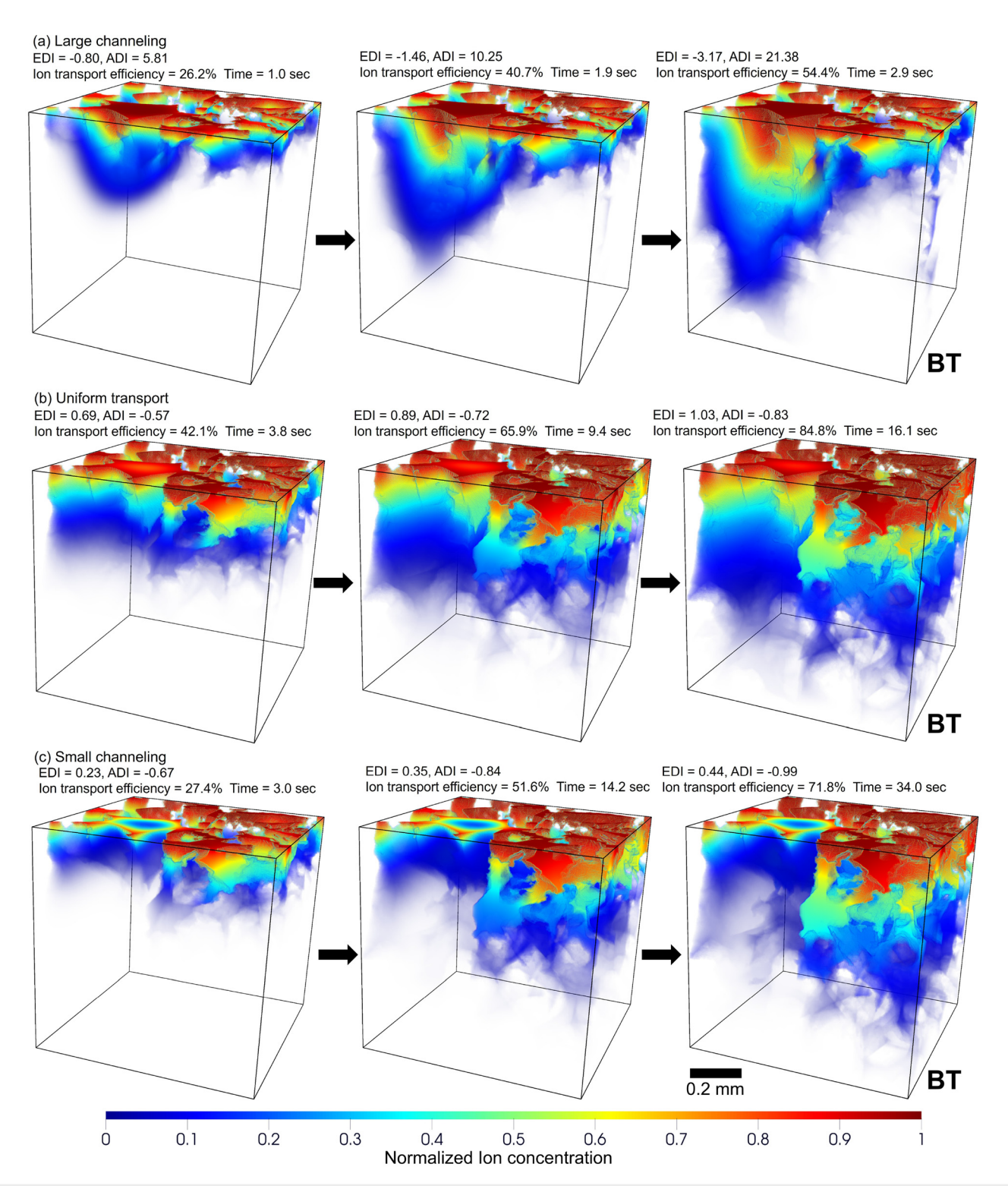


FIG. 8. Ion transport regime for the 3D sandstone micro-CT image (a) large channeling; (b) uniform transport; (c) small channeling. For each transport regime, three time steps are displayed, and the simulation stops when 1% of the ion concentration reaches the outlet (last column), referring to a breakthrough (BT). The ion concentration in each subplot is normalized to 0–1.

example, by replacing flux terms with their Darcy-scale counterparts, forms part of a larger scope of upscaling considerations and model development that is outside the scope of this study. Here, we aim to validate only the fundamental pore-scale model and transport mechanisms in 3D. Upscaling of such work is a significant undertaking that should be considered in the future.

Electrokinetic transport can be applied to a subsurface system to improve the efficiency of ion transport. We find that ion sweep efficiency is high when electrokinetic transport is dominant, e.g., uniform transport, see Figs. 7(c)–7(e) and 8(b) and 8(c); or small channeling, see Figs. 7(f) and 8(c). Such sweep improvement is achieved through a controllable preferential ion transport path by harnessing the interaction between the Electrodiffusivity index and Péclet number. In field implementations, the magnitude of the applied electric potential will be of great importance.⁵⁵ According to our transport regime, the appropriate range of the EDI can be found based on the pressure gradient, the variation in pore size, and the desired transport regime, no matter whether the target zone is located in a low-permeable zone (small channel), high-permeable zone (large channel), or both (uniform transport). Thus, our study theoretically demonstrates the feasibility of controlling the path and direction of ion transport in the subsurface. Achieving such control requires the application of both a specific pressure field and an electric potential. In certain cases, these fields may be applied in opposite directions to each other to control transport patterns. This implies that the active use of work to impede the overall solute transport in a porous system in exchange for a more stable transport front is a viable strategy. The engineering applications of such control are wide-reaching.

In our transport regime map, the small channeling and uniform transport, in most cases, involve advection in the opposite direction of electromigration to counterbalance the ion fluxes in large channels of the porous media. This is intuitively a less efficient system than its counterpart since energy is intentionally wasted. However, in practice, stringent ion flux control is in demand, e.g., for water management and soil remediation. In underground water remediation, the location and dimension of the pollution source are usually unknown. Therefore, a complete cutoff connection between pollution sources and water production wells is desired when the contaminated aguifer is returned to drinking water quality. Under this condition, stringent control of ion transport in the subsurface is more important than the technical efficacy of the implementation scenario.⁵⁶ Therefore, the electrokinetic-advection-diffusion transport approach proposed in this study and the interplay between electromigration and advection transport during small channeling and uniform transport regimes may pose advantages over conventional approaches.

In addition to small channeling and uniform transport, large channeling also needs careful design. For mineral resource recovery technologies, e.g., *in situ* mineral recovery, perfect ion transport control is no longer in demand. Instead, the sweep and time efficiency are of greater importance. A3,58 At the initial stage of recovery, large channeling with pressure-induced advection is desired to efficiently produce the resources that are distributed along and beneath the large channels' surfaces. Afterward, maintaining high pressure will no longer bring a better sweep of ion transport. Adjusting the electric potential on the basis of the transport regime to improve the sweep and transport of ions could bring further economic benefits to the project.

Another important aspect to consider is the effect of late-stage mechanical mixing and dispersion after breakthrough. Dentz et al. Possible focused on the control and improvement of ion transport at the pre-breakthrough and sweeping stages of transport, which are governed by the flow within preferential pathways. This is the dominant factor in overall performance, but it is supplemented and is often a required consideration to account for late-stage mixing and dispersion. To fully account for these influences, further studies on chemical heterogeneity, as well as the already physically heterogeneous domains in our study, may be examined to discern the influence of late-stage mixing.

In general, the observed transport phase diagram results from the complicated interplay between electromigration, advection, and diffusion, which is readily applicable to various engineering problems. Unlike in scaling analysis for fluid flow, where the flow regime would change across a wide range of Peclet numbers (spanning several orders of magnitude), 60-62 for the observed ion transport regimes in Fig. 4, rich behaviors can occur in a narrower range of the ADI and EDI. This demonstrates the importance of controlling pressure and electric potential. Therefore, the relation between these transport mechanisms may also vary over time and space in the process of implementation. One needs to combine our proposed transport regime diagram with specific conditions to design the expected ion transport scenarios. This could be one or a set of targeted transport regimes at each stage of an engineering project. Here, we only consider three transport mechanisms and porous media with contrasting pore sizes; future work on the impact of chemical reactions on the corresponding transport regimes at various scales (e.g., meter scale) would complement our scaling analysis on ion transport under advection-diffusion-electromigration mechanisms.

IV. CONCLUSIONS

We performed a fundamental pore-scale model-based scaling analysis on ion transport within fluid for an advection-diffusion-electromigration system using three different domains with increased complexities, including a 2D microchannel with constant aperture along its paths, 2D synthetic porous media, and a 3D sandstone image with contrasting pore sizes over the simulation domains. The simulations are performed using our open-source solver OPM/LBPM under various advection-diffusion-electromigration conditions. Ion transport regimes are benchmarked using two dimensionless numbers, ADI and EDI, to quantitatively characterize advection flux, diffusion flux, and electromigration flux. Four ion transport regimes are observed and defined based on visual and numerical metrics, which are (1) large channeling, (2) uniform transport, (3) small channeling, and (4) no transport. To facilitate future applications, an advection-diffusionelectromigration transport regime map is established through 40 simulations performed on the 2D microchannel domain. The transport regime map explicitly demonstrates the potential flow regime under various ADI and EDI pairs (both ranging from positive to negative quadrants). A synthetic 2D domain and a 3D sandstone micro-CT image are then used to validate the observed ion transport regimes on the transport regime map and to investigate the pore size variation effects on the ion transport regime. The simulation results highlight that the defined transport regimes observed in our microchannel are also observed in the synthetic 2D domain and the 3D sandstone domain. Furthermore, the breakthrough time of 1% ion concentration is found to be much longer for uniform transport and small

channeling compared to large channeling. This implies there is a trade-off between the enhanced volumetric displacement efficiency via the utilization of different ion transport regimes and the time efficiency of the resulting ion transport through the porous media. Based on these findings, the advection–diffusion–electromigration transport system has the potential for many engineering problems, including, for example, underground water remediation^{63,64} and underground resource recovery, ^{27,65} where the pollutants or target zone can be uniformly distributed in a geological formation or mainly located in low permeable regions. This study herein provides important insights into the implementation strategies of these applications.

A logical next step after investigating the transport regimes is to couple the transport with a geochemical model, such as PhreeqcRM to capture reactive transport. With coupled geochemical reactions, the ion transport behavior could be different because the reaction could change the effective conductivity of the fluid phase, which results in potential implications such as changing fluid chemical properties, local pH, and solubility. Therefore, a third dimensionless number such as the Damkohler number that defines the dissolution needs to be considered. Subsequently, the modeling of heterogeneous systems including clays and other physicochemically diverse porous domains in addition to addressing upscaling considerations to the continuum scale provides a generalized and large-scale framework for electrokinetic ion transport control.

SUPPLEMENTARY MATERIAL

See the supplementary material for details tables summarizing the parameters used through the simulations.

ACKNOWLEDGMENTS

The authors acknowledge the Tyree x-ray CT Facility at the Mark Wainwright Analytical Centre (MWAC) of UNSW, funded by the UNSW Research Infrastructure Scheme, for the acquisition of the 3D micro-CT images.

AUTHOR DECLARATIONS Conflict of Interest

The authors have no conflicts to disclose.

Author Contributions

Kunning Tang: Conceptualization (equal); Data curation (equal); Investigation (lead); Methodology (lead); Software (equal); Validation (equal); Visualization (equal); Writing – original draft (lead). Zhenkai Bo: Conceptualization (equal); Investigation (equal); Methodology (equal); Writing – original draft (supporting); Writing – review & editing (supporting). Zhe Li: Resources (equal); Software (lead); Writing – review & editing (equal). Ying Da Wang: Methodology (equal); Supervision (supporting); Writing – review & editing (equal). James McClure: Software (equal); Supervision (equal); Writing – review & editing (equal). Hongli Su: Investigation (equal); Methodology (equal); Writing – review & editing (equal). Peyman Mostaghimi: Supervision (equal); Writing – review & editing (equal). Ryan T. Armstrong: Conceptualization (equal); Writing – review & editing (equal).

DATA AVAILABILITY

The data that support the findings of this study are openly available in OPM/LBPM at https://doi.org/10.1007/s10596-020-10028-9, Ref. 26 and Micro-CT at http://www.digitalrocksportal.org/projects/421, Ref. 67.

REFERENCES

- ¹D. Jacques, J. Šimnek, D. Mallants, and M. T. van Genuchten, "Multicomponent transport model for variably-saturated porous media: Application to the transport of heavy metals in soils," in *Developments in Water Science* (Elsevier, 2002), Vol. 47, pp. 555–562.
- ²J. W. Delleur, The Handbook of Groundwater Engineering (CRC Press, 2006).
- ³A. Tsitonaki, B. Petri, M. Crimi, H. Mosbaek, R. L. Siegrist, and P. L. Bjerg, "In situ chemical oxidation of contaminated soil and groundwater using persulfate: A review," Crit. Rev. Environ. Sci. Technol. 40(1), 55–91 (2010).
- ⁴G. Taylor, V. Farrington, P. Woods, R. Ring, and R. Molloy, "Review of environmental impacts of the acid *in-situ* leach uranium mining process," in *CSIRO Land and Water Client Report* (CSIRO Clayton, Victoria, 2004).
- ⁵P. Bedrikovetsky and N. Caruso, "Analytical model for fines migration during water injection," Transp. Porous Med. 101, 161–189 (2014).
- ⁶C. P. Nielsen and H. Bruus, "Concentration polarization, surface currents, and bulk advection in a microchannel," Phys. Rev. E 90(4), 043020 (2014).
- ⁷L. Shen and Z. Chen, "Critical review of the impact of tortuosity on diffusion," Chem. Eng. Sci. 62(14), 3748–3755 (2007).
- ⁸R. Sprocati and M. Rolle, "On the interplay between electromigration and electroosmosis during electrokinetic transport in heterogeneous porous media," Water Res. 213, 118161 (2022).
- ⁹R. W. Gillham and J. A. Cherry, "Contaminant migration in saturated unconsolidated geologic deposits," Spec. Pap. Geol. Soc. Am. **189**, 31–62 (1982).
- 10 M. Liu, J. Waugh, S. K. Babu, J. S. Spendelow, and Q. Kang, "Numerical modeling of ion transport and adsorption in porous media: A pore-scale study for capacitive deionization desalination," Desalination 526, 115520 (2022).
- ¹¹M. C. Brooks, E. Yarney, and J. Huang, "Strategies for managing risk due to back diffusion," Groundwater Monit. Rem. 41(1), 76–98 (2021).
- ¹²M. Muniruzzaman and M. Rolle, "Impact of multicomponent ionic transport on pH fronts propagation in saturated porous media," Water Resour. Res. 51(8), 6739–6755, https://doi.org/10.1002/2015WR017134 (2015).
- ¹³A. I. Chowdhury, J. I. Gerhard, D. Reynolds, B. E. Sleep, and D. M. O'Carroll, "Electrokinetic-enhanced permanganate delivery and remediation of contaminated low permeability porous media," Water Res. 113, 215–222 (2017).
- ¹⁴D. D. Runnells and J. L. Larson, "A laboratory study of electromigration as a possible field technique for the removal of contaminants from ground water," Groundwater Monit. Rem. 6(3), 85–91 (1986).
- 15 D. D. Runnells and C. Wahli, "In situ electromigration as a method for removing sulfate, metals, and other contaminants from ground water," Groundwater Monit. Rem. 13(1), 121–129 (1993).
- ¹⁶ A. N. Alshawabkeh, A. T. Yeung, and M. R. Bricka, "Practical aspects of in-situ electrokinetic extraction," J. Environ. Eng. 125(1), 27–35 (1999).
- ¹⁷A. N. Alshawabkeh, "Electrokinetic soil remediation: Challenges and opportunities," Sep. Sci. Technol. 44(10), 2171–2187 (2009).
- ¹⁸P. A. Kler, E. J. López, L. D. Dalcín, F. A. Guarnieri, and M. A. Storti, "High performance simulations of electrokinetic flow and transport in microfluidic chips," Comput. Methods Appl. Mech. Eng. 198(30–32), 2360–2367 (2009).
- ¹⁹J. M. Paz-García, B. Johannesson, L. M. Ottosen, A. B. Ribeiro, and J. M. Rodríguez-Maroto, "Modeling of electrokinetic processes by finite element integration of the Nernst-Planck-Poisson system of equations," Sep. Purif. Technol. 79(2), 183–192 (2011).
- 20 J. Berry, M. R. Davidson, and D. J. Harvie, "A multiphase electrokinetic flow model for electrolytes with liquid/liquid interfaces," J. Comput. Phys. 251, 209-222 (2013).
- ²¹J. López-Herrera, A. Gañán-Calvo, S. Popinet, and M. Herrada, "Electrokinetic effects in the breakup of electrified jets: A volume-of-fluid numerical study," Int. J. Multiphase Flow 71, 14–22 (2015).

- ²²J. Wang, M. Wang, and Z. Li, "Lattice Poisson-Boltzmann simulations of electro-osmotic flows in microchannels," J. Colloid Interface Sci. 296, 729–736 (2006).
- 23H. Yoshida, T. Kinjo, and H. Washizu, "Coupled lattice Boltzmann method for simulating electrokinetic flows: A localized scheme for the Nernst-Plank model," Commun. Nonlinear Sci. Numer. Simul. 19, 3570–3590 (2014).
- ²⁴L. Zhang and M. Wang, "Electro-osmosis in inhomogeneously charged microporous media by pore-scale modeling," J. Colloid Interface Sci. 486, 219–231 (2017).
- ²⁵H. S. Basu, S. S. Bahga, and S. Kondaraju, "A fully coupled hybrid lattice Boltzmann and finite difference method-based study of transient electrokinetic flows," Proc. R. Soc. A 476, 20200423 (2020).
- ²⁶J. E. McClure, Z. Li, M. Berrill, and T. Ramstad (2021). "The LBPM software package for simulating multiphase flow on digital images of porous rocks," OPM/LBPM, https://doi.org/10.1007/s10596-020-10028-9
- ²⁷K. Tang, Z. Li, Y. Da Wang, J. McClure, H. Su, P. Mostaghimi, and R. T. Armstrong, "A pore-scale model for electrokinetic in situ recovery of copper: The influence of mineral occurrence, zeta potential, and electric potential," Transp. Porous Med. 150, 601–626 (2023).
- ²⁸E. Buckingham, "On physically similar systems; Illustrations of the use of dimensional equations," Phys. Rev. 4, 345–376 (1914).
- ²⁹M. Shook, D. Li, and L. W. Lake, "Scaling immiscible flow through permeable media by inspectional analysis," In Situ 16, 311 (1992).
- 30 M. D. Kok, R. Jervis, T. G. Tranter, M. A. Sadeghi, D. J. Brett, P. R. Shearing, and J. T. Gostick, "Mass transfer in fibrous media with varying anisotropy for flow battery electrodes: Direct numerical simulations with 3D X-ray computed tomography," Chem. Eng. Sci. 196, 104–115 (2019).
- ³¹R. Farajzadeh, P. Ranganathan, P. L. J. Zitha, and J. Bruining, "The effect of heterogeneity on the character of density-driven natural convection of CO₂ overlying a brine layer," Adv. Water Resour. 34(3), 327–339 (2011).
- ³²G. Wang, G. Pickup, K. Sorbie, and E. Mackay, "Scaling analysis of hydrogen flow with carbon dioxide cushion gas in subsurface heterogeneous porous media," Int. J. Hydrogen Energy 47(3), 1752–1764 (2022).
- 33 D. Li and L. W. Lake, "Scaling fluid flow through heterogeneous permeable media," SPE Adv. Technol. Ser. 3(01), 188–197 (1995).
- 34 H. P. Menke, J. Maes, and S. Geiger, "Channeling is a distinct class of dissolution in complex porous media," Sci. Rep. 13(1), 11312 (2023).
- 35A. Metzner and J. Reed, "Flow of non-newtonian fluids—correlation of the laminar, transition, and turbulent-flow regions," Aiche J. 1(4), 434–440 (1955).
- 36H. P. Menke, Reservoir Condition Pore-Scale Imaging of Reaction (Imperial College London, 2016).
- 37H. Dawood, H. A. Mohammed, N. A. C. Sidik, K. M. Munisamy, and M. Wahid, "Forced, natural and mixed-convection heat transfer and fluid flow in annulus: A review," Int. Commun. Heat Mass Transfer 62, 45–57 (2015).
- ³⁸M. J. Patel, E. F. May, and M. L. Johns, "High-fidelity reservoir simulations of enhanced gas recovery with supercritical CO₂," Energy 111, 548–559 (2016).
- 39 T. J. Hughes, A. Honari, B. F. Graham, A. S. Chauhan, M. L. Johns, and E. F. May, "CO₂ sequestration for enhanced gas recovery: New measurements of supercritical CO₂–CH₄ dispersion in porous media and a review of recent research," Int. J. Greenhouse Gas Control 9, 457–468 (2012).
- ⁴⁰S. Higgs, Y. Da Wang, C. Sun, J. Ennis-King, S. J. Jackson, R. T. Armstrong, and P. Mostaghimi, "Comparative analysis of hydrogen, methane and nitrogen relative permeability: Implications for underground hydrogen storage," J. Energy Storage 73, 108827 (2023).
- 41M. Boon and H. Hajibeygi, "Experimental characterization of H₂/water multiphase flow in heterogeneous sandstone rock at the core scale relevant for underground bydrogen storage (UHS)." Sci. Rep. 12, 14604 (2022).
- ground hydrogen storage (UHS)," Sci. Rep. 12, 14604 (2022).

 42 R. Lenormand, E. Touboul, and C. Zarcone, "Numerical models and experiments on immiscible displacements in porous media," J. Fluid Mech. 189, 165–187 (1988).
- ⁴³E. Martens, H. Prommer, R. Sprocati, J. Sun, X. Dai, R. Crane, J. Jamieson, P. O. Tong, M. Rolle, and A. Fourie, "Toward a more sustainable mining future with electrokinetic in situ leaching," Sci. Adv. 7(18), eabf9971 (2021).
- ⁴⁴X.-H. Ding, S.-J. Feng, and Q.-T. Zheng, "Forward and back diffusion of reactive contaminants through multi-layer low permeability sediments," Water Res. 222, 118925 (2022).
- ⁴⁵C. V. Deutsch and A. G. Journel, GSLIB: Geostatistical Software Library and User's Guide (Oxford University Press, 1992), Vol. 8.

- ⁴⁶M. Kühn, C. Niewöhner, M. Isenbeck-Schröter, and H. Schulz, "Determination of major and minor constituents in anoxic thermal brines of deep sandstone aquifers in Northern Germany," Water Res. 32(2), 265–274 (1998).
- ⁴⁷M. S. de Melo, G. B. Guimaraes, A. L. Chinelatto, P. C. F. Giannini, H. S. Pontes, A. S. A. Chinelatto, and D. Atencio, "Kaolinite, illite and quartz dissolution in the karstification of Paleozoic sandstones of the Furnas Formation, Paraná Basin, Southern Brazil," J. South Am. Earth Sci. 63, 20–35 (2015).
- ⁴⁸M. Mohamaden, A. Wahaballa, and H. El-Sayed, "Application of electrical resistivity prospecting in waste water management: A case study (Kharga Oasis, Egypt)," Egypt. J. Aquat. Res. 42(1), 33–39 (2016).
- ⁴⁹ K. Tang, Y. Da Wang, J. McClure, C. Chen, P. Mostaghimi, and R. T. Armstrong, "Generalizable framework of unpaired domain transfer and deep learning for the processing of real-time synchrotron-based x-ray microcomputed tomography images of complex structures," Phys. Rev. Appl. 17(3), 034048 (2022).
- ⁵⁰S. Ray, D. Mondal, and S. Reuveni, "Péclet number governs transition to acceleratory restart in drift-diffusion," J. Phys. A 52(25), 255002 (2019).
- ⁵¹B. J. Kirby and E. F. Hasselbrink, Jr., "Zeta potential of microfluidic substrates: 1. Theory, experimental techniques, and effects on separations," Electrophoresis 25(2), 187–202 (2004).
- ⁵²J. A. A. Júnior and J. B. Baldo, "The behavior of zeta potential of silica suspensions," New J. Glass Ceram. 4(2), 29 (2014).
- ⁵³Z. Jangda, H. Menke, A. Busch, S. Geiger, T. Bultreys, H. Lewis, and K. Singh, "Pore-scale visualization of hydrogen storage in a sandstone at subsurface pressure and temperature conditions: Trapping, dissolution and wettability," J. Colloid Interface Sci. 629, 316–325 (2023).
- ⁵⁴J. B. Roerdink and A. Meijster, "The watershed transform: Definitions, algorithms and parallelization strategies," Fundam. Inf. 41(1-2), 187-228 (2000).
- 55R. Sprocati, M. Masi, M. Muniruzzaman, and M. Rolle, "Modeling electrokinetic transport and biogeochemical reactions in porous media: A multidimensional Nernst-Planck-Poisson approach with PHREEQC coupling," Adv. Water Resour. 127, 134-147 (2019).
- ⁵⁶D. M. Mackay and J. A. Cherry, "Groundwater contamination: Pump-and-treat remediation," Environ. Sci. Technol. 23, 630–636 (1989).
- 57A. Lima, A. Hofmann, D. Reynolds, C. Ptacek, P. Van Cappellen, L. M. Ottosen, S. Pamukcu, A. Alshawabekh, D. O'Carroll, C. Riis et al., "Environmental electrokinetics for a sustainable subsurface," Chemosphere 181, 122–133 (2017).
- ⁵⁸G. Wang, J. Xu, L. Ran, R. Zhu, B. Ling, X. Liang, S. Kang, Y. Wang, J. Wei, L. Ma *et al.*, "A green and efficient technology to recover rare earth elements from weathering crusts," Nat. Sustainable 6, 81–12 (2022).
- ⁵⁹M. Dentz, T. Le Borgne, A. Englert, and B. Bijeljic, "Mixing, spreading and reaction in heterogeneous media: A brief review," J. Contam. Hydrol. 120–121, 1–17 (2011).
- ⁶⁰H. P. Menke, "Reservoir condition pore-scale imaging of reaction," Ph.D. thesis (Imperial College London, 2015).
- 61A. Adrover and S. Cerbelli, "Laminar dispersion at low and high Peclet numbers in finite-length patterned microtubes," Phys. Fluids 29(6), 062005 (2017)
- ⁶²K. Yang, M. Li, N. N. Ling, E. F. May, P. R. Connolly, L. Esteban, M. B. Clennell, M. Mahmoud, A. El-Husseiny, A. R. Adebayo *et al.*, "Quantitative tortuosity measurements of carbonate rocks using pulsed field gradient NMR," Transp. Porous Med. **130**, 847–865 (2019).
- ⁶³L. Malaeb and G. M. Ayoub, "Reverse osmosis technology for water treatment: State of the art review," <u>Desalination</u> 267(1), 1–8 (2011).
- ⁶⁴X. Liu, F. Ma, H. Zhu, X. Ma, J. Guo, X. Wan, L. Wang, H. Wang, and Y. Wang, "Effects of magnetized water treatment on growth characteristics and ion absorption, transportation, and distribution in *Populus × euramericana* 'Neva' under NaCl stress," Can. J. Res. 47(6), 828–838 (2017).
- ⁶⁵E. Karami, L. Kuhar, A. Bona, and A. N. Nikoloski, "A review of electrokinetic, ultrasonic and solution pulsing methods for mass transfer enhancement in insitu processing," Miner. Eng. 170, 107029 (2021).
- ⁶⁶D. L. Parkhurst and L. Wissmeier, "PhreeqcRM: A reaction module for transport simulators based on the geochemical model PHREEQC," Adv. Water Resour. 83, 176–189 (2015).
- ⁶⁷Y. Cui, C. Arns, and I. Shikhov (2022). "3D sandstone sample images," Micro-CT, http://www.digitalrocksportal.org/projects/421